Observations of the Flow Field near the Nose of a Buoyant Coastal Current*

STEVEN J. LENTZ AND STEVE ELGAR

Woods Hole Oceanographic Institution, Woods Hole, Massachusetts

R. T. GUZA

Scripps Institution of Oceanography, La Jolla, California

(Manuscript received 30 May 2002, in final form 4 November 2002)

ABSTRACT

Low-salinity water from Chesapeake Bay forms an intermittent buoyant gravity current that propagates more than 100 km southward along the coast. During five events when wind and surface gravity-wave forcing were weak, the buoyant coastal current 90 km south of Chesapeake Bay was less than 5 km wide, was 5–10 m thick, and propagated alongshore at ~50 cm s^{-1}. The density decreased 2–3 kg m^{-3} over a few hundred meters at the nose of the buoyant coastal current, which was located about 1 km offshore in ~8 m of water. Water up to 4 km ahead of the advancing nose was displaced southward and offshore (maximum velocities near the nose of 20 and 10 cm s^{-1}, respectively). The southward alongshore current increased abruptly to ~50 cm s^{-1} at the nose and continued to increase to a supercritical maximum of ~70 cm s^{-1} about 1 km behind the nose. An onshore flow of between 5 and 15 cm s^{-1}, which extended at least 5 km behind the nose, supplied buoyant water to the onshore region of weak, subcritical alongshore flow. The observed flow structure is qualitatively similar to theoretical predictions and laboratory measurements of buoyant gravity currents propagating along a sloping bottom.

1. Introduction

Buoyant water discharged onto continental shelves by estuaries and rivers typically turns anticyclonically (to the right in the Northern Hemisphere) and forms a narrow, shallow gravity current that can propagate tens to hundreds of kilometers along the coast. Although buoyant coastal currents influence a range of continental shelf processes (Hill 1998), the associated flow field is not understood well. Here, flows associated with buoyant coastal currents observed 90 km south of Chesapeake Bay during periods of weak winds and low-energy surface gravity waves are discussed.

In laboratory and modeling studies of buoyant gravity currents propagating along a vertical wall over a flat bottom in a rotating frame, the flow parallel to the wall (alongshore) behind the nose of the gravity current is geostrophic and reaches a maximum near the wall (Fig. 1a; Stern et al. 1982; Griffiths and Hopfinger 1983). Near the nose, the flow turns offshore. In a reference frame moving with the propagating gravity current (Fig. 1a, lower panel), the alongshore flow behind the nose is toward the nose in the onshore part of the current (e.g., near the wall) and away from the nose farther offshore. In laboratory studies, the gravity current is spread laterally by instabilities that develop behind the turbulent nose.

Laboratory and numerical modeling studies indicate that buoyant gravity currents over sloping and flat bottoms are different (Whitehead and Chapman 1986; Chao 1988; Chapman and Lentz 1994; Kourafalou et al. 1996; Yankovsky and Chapman 1997; Garvine 1999; Fong and Geyer 2002; Lentz and Helfrich 2002). In two laboratory studies, buoyant gravity currents over a sloping bottom were wider, were more stable, and propagated more slowly than gravity currents (with similar source transport, density anomaly, and rotation rate) over a flat bottom adjacent to a vertical wall (Whitehead and Chapman 1986; Lentz and Helfrich 2002).

According to a simple theory (Lentz and Helfrich 2002), the geostrophic, alongshore flow behind the nose is concentrated at the density front separating the buoyant current from the ambient fluid, and this alongshore flow is faster than the nose propagation speed (i.e., supercritical; Fig. 1b). Cross-shore density gradients and alongshore flow are assumed to be weak onshore of the density front, and this region is supplied with buoyant

* Woods Hole Oceanographic Institution Contribution Number 10748.

Corresponding author address: Steven J. Lentz, Department of Physical Oceanography, Woods Hole Oceanographic Institution, Woods Hole, MA 02543.
E-mail: slentz@whoi.edu

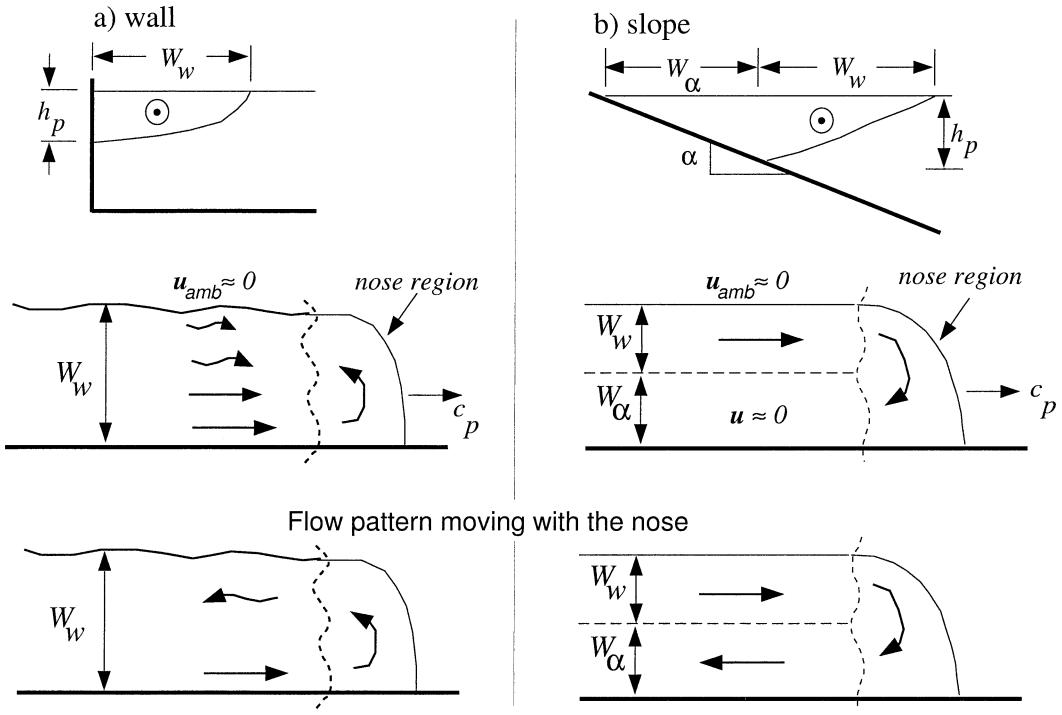

FIG. 1. Schematics of flow patterns of buoyant gravity currents propagating (a) over a flat bottom with a vertical wall (Griffiths and Hopfinger 1983) and (b) over a sloping bottom (Lentz and Helfrich 2002). (top) Cross sections of the flow behind the nose. Flow is out of the page. The thin solid curves indicate a sharp density front separating the buoyant plume from the ambient fluid at rest. (middle) Plan views of the flow field. A thin viscous boundary layer near the wall is not shown. (bottom) Plan views of the flow field in a reference frame moving at c_p, the nose propagation speed. The cross-shore distance from the location at which the density front intersects the bottom (or the wall) to the offshore edge of the gravity current plume (at the surface) is W_w. For a sloping bottom, the maximum plume thickness h_p occurs where the plume intersects the bottom, a distance W_α from the coast.

water by an onshore flow behind the nose (Fig. 1b, middle panel). In a coordinate frame moving with the nose, the alongshore flow over a slope is away from the nose near the coast and toward the nose farther offshore, opposite to the pattern over a flat bottom with a vertical wall (cf. the two lower panels in Fig. 1 with each other). Laboratory observations of buoyant gravity currents over a sloping bottom are similar to the theoretical predictions (Lentz and Helfrich 2002), with alongshore flow reaching a maximum near where the front intersects the bottom and weak (although not zero as predicted) alongshore flow onshore of the maximum flow.

Previous oceanographic observational studies have characterized the flow field near the source of a buoyant outflow (Luketina and Imberger 1987; O'Donnell et al. 1998; Marmorino and Trump 2000), but detailed observations of the nose region of a buoyant coastal current are rare (Rennie et al. 1999; Yankovsky et al. 2000; Johnson et al. 2001; Donato and Marmorino 2002). Here, the flow and density fields observed near the nose of buoyant coastal currents emanating from Chesapeake Bay are shown to resemble results from theory and laboratory studies (Fig. 1b).

2. Background

a. Measurements and processing

Current, salinity, and temperature observations were obtained from August to October of 1994 along a cross-shore transect located approximately 90 km south of Chesapeake Bay (Fig. 2). Vertical stacks of electromagnetic current meters were deployed on towers in 2-, 4-, and 8-m mean water depth, and vector-measuring current meters were deployed on moorings in 13- and 21-m water depth (Fig. 2b). The current meters spanned most of the water column at each site, although the shallowest current meter was 4 m below the surface at the 13- and 21-m sites. The estimated accuracy of the current measurements is 2–3 cm s^{-1} (Beardsley 1987; Guza et al. 1988). Salinity observations were obtained from temperature and conductivity instruments spanning the water column at the 13- and 21-m sites (Fig. 2b) and at two levels below the surface at the U.S. Army Corps of Engineers Field Research Facility (FRF) pier in 7-m water depth. The upper temperature and conductivity instruments were 4 m below the surface at the pier site and 2 m below the surface at the 13- and 21-m sites. The 2-, 4-, and 8-m

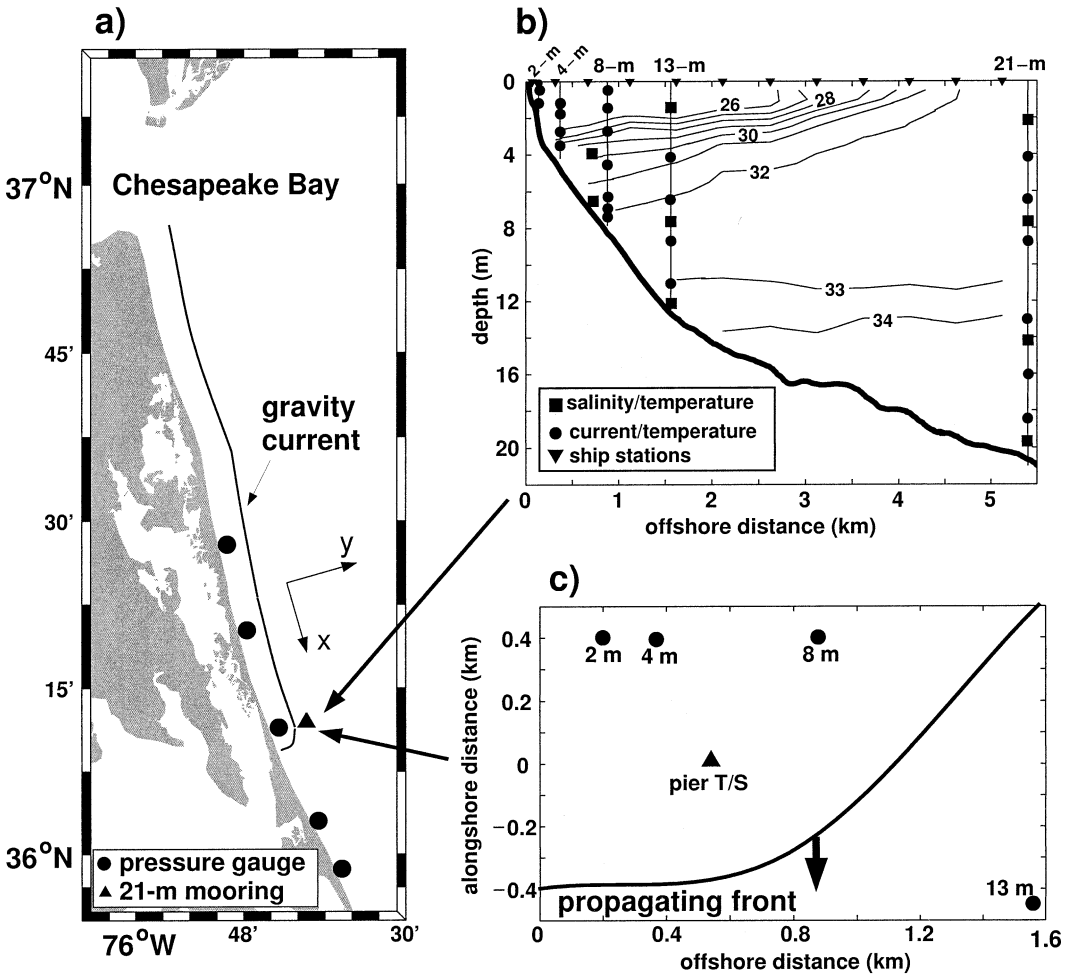

FIG. 2. Schematics of the buoyant coastal current and the instrument arrays. (a) Plan view of the study area showing a buoyant coastal current and the alongshore array of pressure–temperature–conductivity instruments deployed along the 5-m isobath with approximately 15-km spacing. (b) Vertical and cross-shore locations of the instrumented cross-shore transect superimposed on the cross-shore salinity structure observed (courtesy of J. Largier) during buoyant coastal current event 3 (see Fig. 3). (Salinity values are based on the practical salinity scale.) (c) Expanded plan view of the instrument sites and the inferred front geometry.

sites were on a transect perpendicular to the coast, whereas the pier and 13-m sites were about 400 and 850 m southeast (alongshore), respectively, of the transect (Fig. 2c). Wind was measured at the end of the FRF pier, and surface waves were measured near the 8-m site. An alongshore array of five temperature–conductivity–pressure instruments spaced approximately 15 km apart in 5-m mean water depth was centered on the cross-shore transect of current meters (Fig. 2a). See Elgar et al. (1997), Feddersen et al. (1998), Lentz et al. (1999), and Rennie et al. (1999) for additional details.

Temperature and salinity measurements from the alongshore array in 5-m depth (Fig. 2a) and the 13-m, 21-m, and pier sites are instantaneous samples obtained every 4 min. The other observations were averaged into 4-min values. Current and wind observations were rotated into an alongshore (x positive toward 160°T), cross-shore (y positive offshore) coordinate frame (Fig. 2a). Tidal velocities near the coast in this region are a few centimeters per second (Lentz et al. 2001), much weaker than the flows associated with the buoyant coastal current.

b. Buoyant current events

Buoyant coastal currents occur when variations in winds at the mouth of Chesapeake Bay release buoyant estuarine water (Rennie 1997). Nine buoyant coastal current events were observed between 16 August and 3 October 1994, when near-surface measurements were available at the 8- or 13-m sites (Table 1 and Fig. 3; Rennie et al. 1999). The arrival of the nose of the buoyant coastal current is defined by an abrupt decrease in the near-surface salinity at the pier site (water depth 7 m; Fig. 3d). No consistent pattern of temperature var-

TABLE 1. Characteristics of the buoyant coastal current nose during the nine events identified in Fig. 3, including the time that the nose arrives at the pier site, the estimated propagation speed of the nose c_{obs}, and the density decrease across the front $\Delta\rho$. Ambient shelf conditions 2 h prior to the arrival of the nose also are noted, including the alongshore (τ^{sx}) and cross-shore (τ^{sy}) components of the wind stress at the pier, the significant wave height H_{sig} near the 8-m site, and the near-surface, alongshore velocity at the 8-m (u^{8}_{amb}) and 13-m (u^{13}_{amb}) sites. Alongshore wind stresses and significant wave heights were small prior to events 1–5 and were larger prior to events 6–9.

No.	Time (UTC)	c_{obs} (cm s^{-1})	$\Delta\rho$ (kg m^{-3})	τ^{sx} (Pa)	τ^{sy} (Pa)	H_{sig} (m)	u^{8}_{amb} (cm s^{-1})	u^{13}_{amb} (cm s^{-1})
1	1605 Aug 16	55	2.1	0.01	−0.07	0.54	−21	−9
2	3300 Aug 20	56	2.4	0.00	0.00	0.33	5	10
3	7250 Aug 31	55	3.1	0.00	−0.02	0.40	−11	−12
4	2255 Sep 8	45	1.8	0.00	−0.02	0.45	—	−2
5	7580 Sep 30	49	2.2	0.02	0.02	0.46	−10	−14
6	1348 Aug 23	55	1.6	0.09	−0.03	1.28	52	51
7	1934 Sep 2	65	1.9	0.02	−0.08	0.94	28	35
8	1926 Sep 19	49	2.1	0.08	−0.07	1.45	33	31
9	2318 Oct 3	64	1.0	0.22	−0.14	2.32	48	38

iation was associated with the buoyant plumes (not shown), and the density is salinity controlled.

The alongshore propagation speed c_{obs} of the nose, estimated as the separation (34 km) between the instruments north and south of the central transect (Fig. 2a) divided by the difference in nose arrival time (Rennie et al. 1999), was between 45 and 65 cm s^{-1} (Table 1). Similar propagation speeds were observed in a study of the Chesapeake Bay plume during 1997 (Johnson et al. 2001).

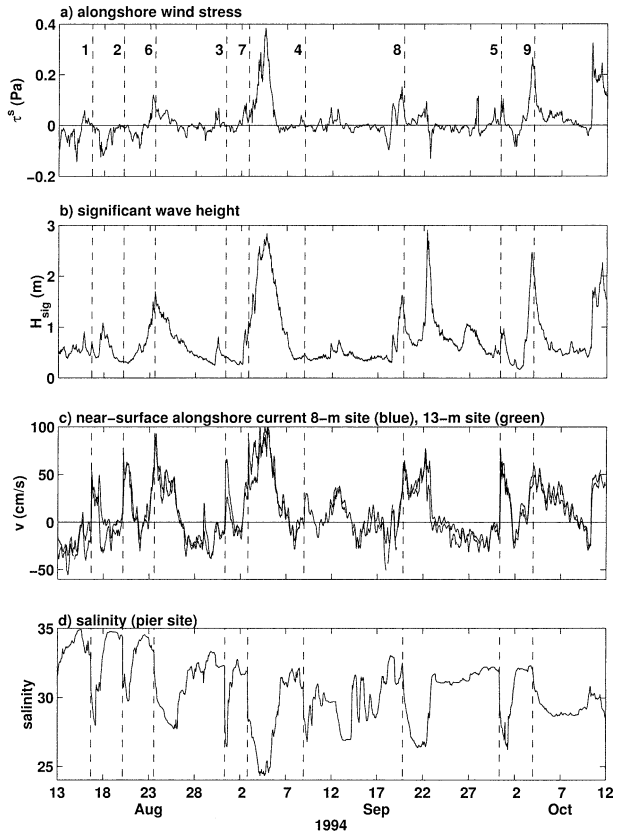

FIG. 3. (a) Alongshore wind stress (τ^{sx}) at the FRF pier, (b) significant wave height (H_{sig}) in 8-m water depth, (c) alongshore current (u) 1.4 m below the surface in 8-m water depth, and (d) salinity (practical salinity scale) 4 m below the surface at the FRF pier in 7-m water depth vs time. Positive τ^{sx} and u are southward alongshore. Nine buoyant gravity current events are numbered and are marked by the vertical dashed lines. The wind stress and significant wave height were small prior to events 1–5.

During five events (events 1–5 in Table 1 and Fig. 3), alongshore wind stresses and significant wave heights were small preceding the nose arrival. Ambient alongshore currents (approximately 2 h prior to the salinity front arrival) were weak or northward (opposing the alongshore propagation of the buoyant current). Each of these five plumes propagated past the most southern instrument in the alongshore array (30 km south of the cross-shore transect). During the other four events (6–9), ambient wind and breaking-wave-driven alongshore currents were relatively strong in the direction of the buoyant current propagation (Feddersen et al. 1998; Lentz et al. 1999). Here, the focus is on the buoyancy-dominated events 1–5.

Temporal variations in current and salinity as the buoyant current nose propagates past the cross-shore array are assumed to result from the alongshore advection of features (at speed c_{obs}) that are changing slowly in time. The structure of the salinity front does not change significantly during the approximately 30 h required to traverse the 60-km-long alongshore array (Fig. 2a) at $c_{obs} = 50$ cm s^{-1} (Rennie et al. 1999). As a consequence, the spatial structure of flow in the nose region is assumed to be constant for approximately 10 h near the time of front arrival. For $c_{obs} \approx 50$ cm s^{-1}, the front moves 120 m between 4-min samples, and so alongshore scales greater than about 100 m are resolved. The pier and 13-m sites are 400 and 850 m downstream (i.e., south) of the 2-, 4-, and 8-m sites (Fig. 2c), and so the pier and 13-m site time series are shifted 12 (3 samples) and 24 min (six samples), respectively, to account roughly for the lag in front arrival. Observed velocity time series are converted to alongshore spatial variations using the observed nose propagation speed c_{obs} (Table 1), with the time origin corresponding to the arrival time (t_o) of the salinity front at the pier site. In

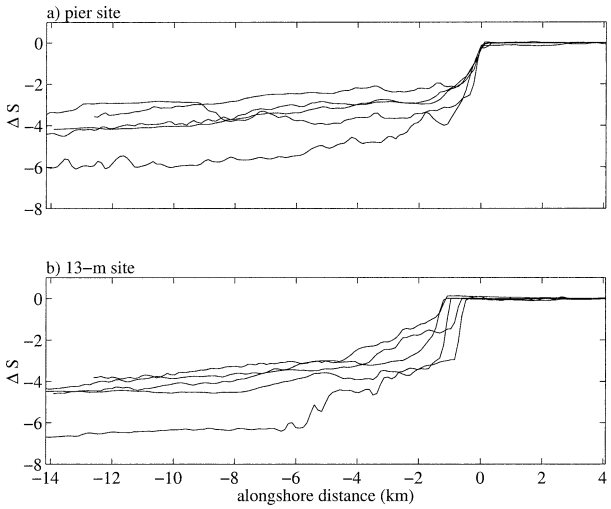

FIG. 4. Relative salinity ΔS vs alongshore distance for events 1–5 at the (a) pier (4 m below the surface) and (b) 13-m (1.5 m below the surface) sites. Alongshore variation is estimated from observed temporal variations by assuming advection at the front propagation speed [c_{obs}; (1)]. (Time increases from right to left.) For each event the origin (alongshore distance = 0) is defined by the arrival of the salinity front at the pier site, and the salinities are relative to values ~4 km downstream from the front [(1)]. The salinity drop at the 13-m site lags the drop at the pier site by about 1 km as depicted schematically by the curve labeled ''propagating front'' in Fig. 2c.

addition, the ambient value of the current observed at each site ~2 h prior to the front arrival (denoted as t_{4km}, 4 km ahead of the nose; Table 1) is subtracted from the spatial series. For example, the alongshore velocity u as a function of alongshore location x is estimated as

$$u(x) = u(t = t_o - x/c_{obs}) - u(t_o - t_{4km}). \qquad (1)$$

3. Buoyant current characteristics

a. Spatial structure of the buoyant plumes

At the 8- and 13-m sites, the nose arrival is characterized by a salinity decrease of 2–4 over 8–40 min (the corresponding frontal width is 240–1200 m; Fig. 4) that gradually increases to 4–6 and persists between 1 and 4 days (Fig. 3d). The leading edge of the plume curves such that the front arrives at the 13-m site about 40 min later than at the pier (after adjustment for the relative alongshore locations), corresponding to an alongshore lag of about 1 km (Figs. 4 and 2c).

Small-boat and larger-scale hydrographic sections obtained during weak winds and low waves (e.g., event 3; Fig. 2b) indicate that the plume width was 4–5 km and that the front intersected the seafloor between the 5- and 10-m isobaths (i.e., about 1 km offshore) (Rennie et al. 1999). Plume widths of about 5 km also were observed during weak winds in 1997 (Johnson et al. 2001). These results are consistent with the present observation that the low-salinity plume extended nearly to the seafloor at the pier site (water depth of 7 m), was about 7–8 m thick at the 13-m site, and was not observed at the 21-m site (5.6 km offshore) until after the onset of either offshore or upwelling-favorable (northward) winds that dispersed the buoyant coastal current offshore. The currents observed at the 8- and 13-m sites during events 1–5 (discussed below) also are consistent with a plume thickness of 7–8 m.

During events 1 and 4, temperatures and salinities from the 13-m site suggest that the plume was thickest near the nose (not shown). This borelike structure, with thinning behind the nose, is similar to laboratory observations of buoyant gravity currents along a wall (Stern et al. 1982; Griffiths and Hopfinger 1983) and to field observations of small buoyant plumes near a source (Luketina and Imberger 1987; O'Donnell et al. 1998). In the other three events, the plume thickness increased with distance behind the nose.

b. Flow field

The inferred alongshore structure of the near-surface flow field, relative to the ambient alongshore flow, is similar for events 1–5 (Figs. 5 and 6). The arrival of the salinity front (alongshore distance $x \sim 0$ at the 2-, 4-, and 8-m sites and $x \sim -1$ km at the 13-m site; Figs. 2c and 4) is preceded by near-surface alongshore flow (above ambient) in the direction of the plume propagation that increases approximately linearly from zero about 4 km (2.2 h) ahead of the front to 10–20 cm s^{-1} just ahead of the front (Fig. 5). At the front, the near-surface alongshore velocity at the 8-m site increases over a few hundred meters to 40–60 cm s^{-1}, approximately the front propagation speed c_{obs}, as expected if the front is a material surface. Alongshore velocity increases are less abrupt and are smaller at the other sites, although an abrupt velocity increase is observed at the 13-m site during event 1. Changes in velocity close to the surface at the 13-m site could not be detected because the shallowest current meter was 4 m below the surface. Near-surface offshore flow (maximum ~5–15 cm s^{-1}) is observed just ahead of, and at, the front (Figs. 6b–d). This offshore flow weakens as the distance from shore decreases and usually is not detectable at the 2-m site (Fig. 6). The near-surface flow ahead of the front suggests the advancing buoyant plume displaces water ahead of it in both the downstream and offshore directions, qualitatively similar to the potential flow ahead of a translating, semi-infinite blunt body (e.g., Batchelor 1981).

Behind the front, the near-surface alongshore currents continue to increase and reach peak velocities (relative to the ambient flow) of 10–20 (at the 2-m site), 30–50 (4-m site), 75–100 (8-m site), and 40–80 cm s^{-1} (13-m site) (Fig. 5). Peak near-surface alongshore currents occur farther behind the salinity front at the 13-m site than in shallower depths. Maximum alongshore currents are supercritical (~$1.5c_{obs}$ for events 1–4 and ~$2c_{obs}$ for event 5) at the 8-m site, are usually slightly subcritical

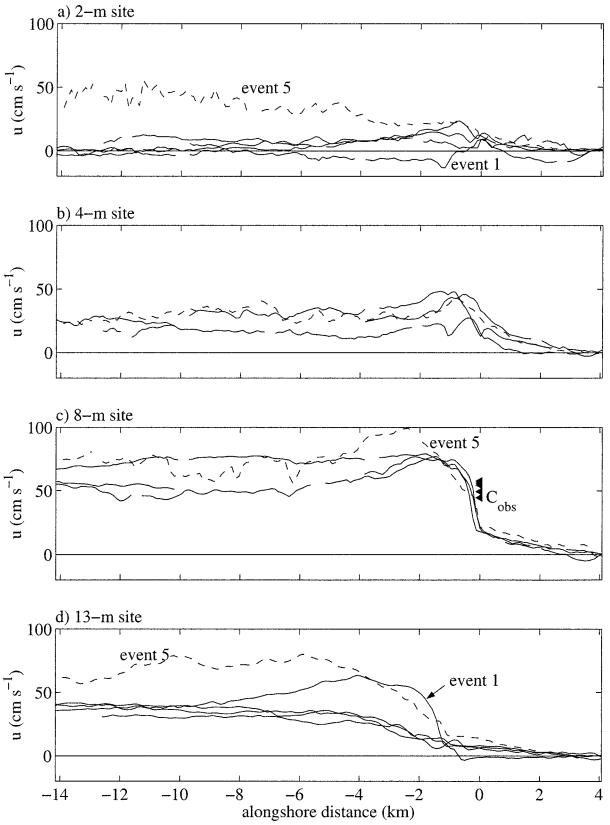

FIG. 5. Near-surface alongshore velocity (positive flow is southward) vs alongshore distance for events 1–5 at the (a) 2- (0.4 m below the surface), (b) 4- (2.0 m below the surface), (c) 8- (1.7 m below the surface), and (d) 13-m (4.2 m below the surface) sites. For each event, the origin (alongshore distance = 0) is defined by the arrival of the salinity front at the pier site (7-m water depth, 4.0 m below the surface), advection at c_{obs} is assumed, and the velocities are relative to values ~4 km downstream from the front [(1)]. The value of c_{obs} for each event is noted in (c) at the alongshore distance equal to 0. (Time increases from right to left.)

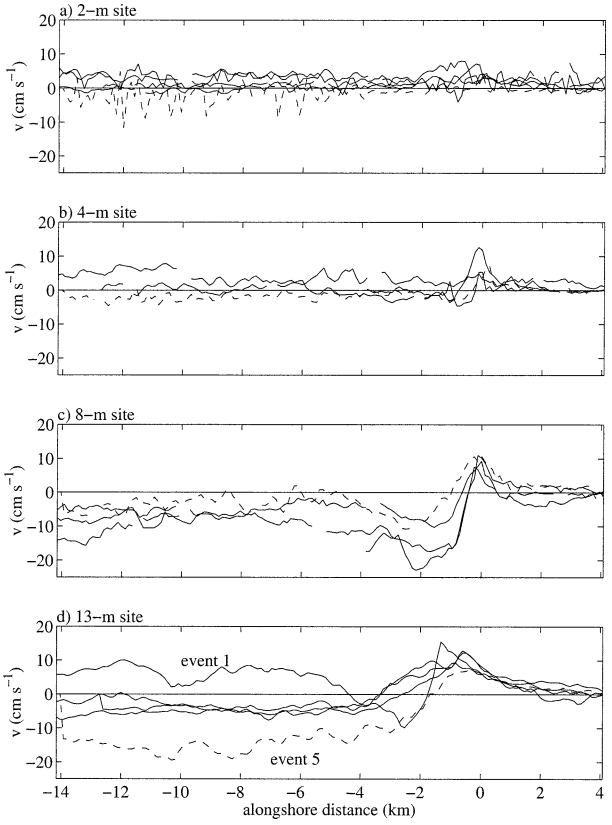

FIG. 6. As in Fig. 5 but for near-surface cross-shore velocity (positive flow is offshore).

($\sim$0.8–0.9c_{obs}) at the 4-m site, and are always subcritical at the 2-m site. At the 13-m site, peak currents 4 m below the surface are supercritical in events 1 and 5 and are slightly subcritical during the other events. The larger near-surface alongshore currents at the 2-, 8-, and 13-m sites during event 5 (dashed curve in Fig. 5) probably were caused by moderate alongshore wind stresses (0.1 Pa) in the direction of the front propagation and (at the 2-m site) obliquely incident breaking surface waves (significant wave heights were approximately 1 m) shortly after the front passed (Figs. 3a, b). (Values listed in Table 1 are prior to arrival of the nose.) The alongshore current usually decreased by 10–20 cm s^{-1} about 5 km behind the location of the maximum value, except at the 13-m site, where the alongshore current continued to increase gradually behind the nose. Near-surface alongshore currents at all except the 2-m site typically persisted for the 1–2-day duration of the event (Fig. 3, equivalent to a 40–80 km alongshore displacement for c_{obs} = 50 cm s^{-1}). Rennie et al. (1999) discuss the evolution of these plume events over these longer timescales. At the 8- and 13-m sites, onshore flow of between 5 and 15 cm s^{-1} extends at least 5 km behind the nose (Figs. 6c,d) and provides buoyant water to the onshore region of weak, subcritical alongshore flow (Figs. 5a,b). Behind the front at the 13-m site, the 5–10 cm s^{-1} offshore flow during event 1 and the anomalously large onshore flow during event 5 (Fig. 6d) are both consistent with estimates of the corresponding wind-driven cross-shelf velocities (Ekman transport divided by the plume thickness; Fig. 3a; Lentz 2001).

Within approximately the upper 8 m of the water column, passage of the front is accompanied by increases in the alongshore flow (Fig. 7) and by cross-shore flow reversals (Figs. 8b,c), similar to the near-surface flow (Figs. 5 and 6). The maximum offshore flow at the 4- and 8-m sites occurs near the bottom, beneath the leading edge of the front ($-2 > x > 0$ km), and the cross-shore flow is vertically sheared in this region. At the 13-m site, the cross shore flow near the front exhibits less vertical shear. Behind the front, the alongshore flow decreases with increasing distance below the surface (Fig. 7), and at the 13-m site the alongshore flow reverses near the seafloor (e.g., the -10 cm s^{-1} flow extending about 5 km behind the front; Fig. 7c). Temperature variations (not shown) suggest that in some

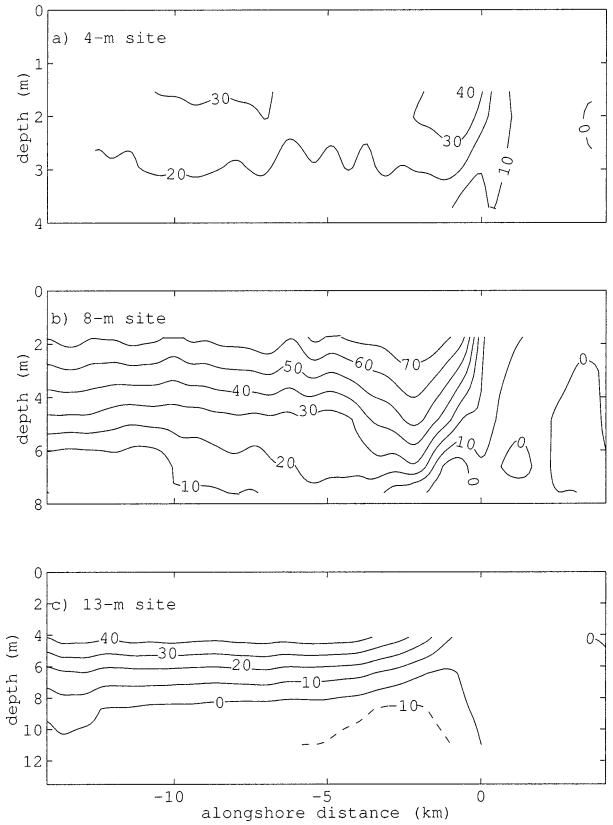

FIG. 7. Contours of alongshore velocity (cm s^{-1}) averaged over events 1–5 (positive flow is southward) as a function of distance below the surface and alongshore distance at the (a) 4-, (b) 8-, and (c) 13-m sites. For each event, the origin (alongshore distance = 0) is defined by the arrival of the salinity front at the pier site (7-m depth), advection at c_{obs} is assumed, and the velocities are relative to values ~4 km downstream from the front [(1)]. (Time increases from right to left.)

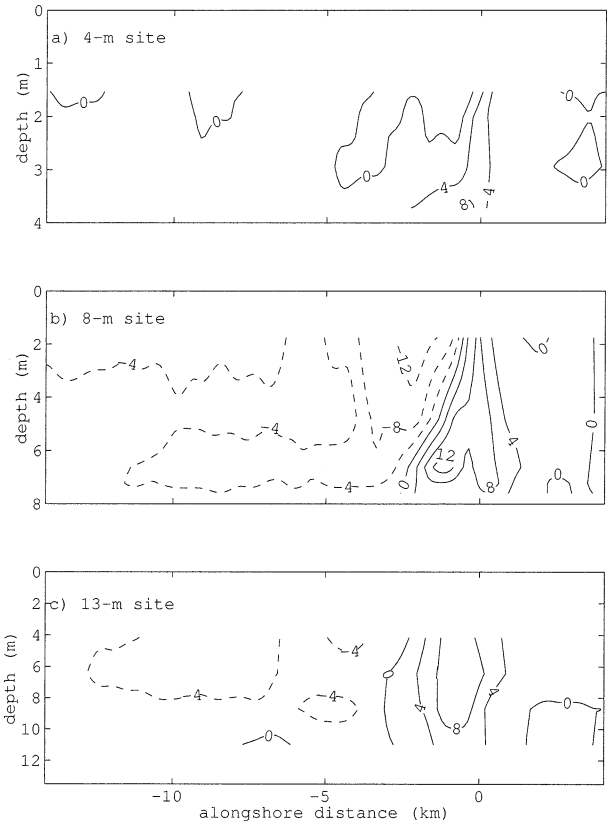

FIG. 8. As in Fig. 7 but for contours of cross-shore velocity (cm s^{-1}; positive flow is offshore).

cases warm surface water is subducted below the buoyant plume water.

c. Dynamical balances

The observations allow estimation of terms in the alongshore and cross-shore momentum balances. A translating coordinate frame (x', y', z') moving at the propagation speed c_{obs} is used, so $x' = x - c_{\text{obs}}t$ and $u' = u - c_{\text{obs}}$($t' = t, y' = y$, and $z' = z$). The total derivative is invariant to this Galilean transformation, and thus

$$u_t + uu_x + vu_y + wu_z = u'_{t'} + u'u'_{x'} + v'u'_{y'} + w'u'_{z'}.$$

The steady cross- and alongshore momentum balances in the translating coordinate frame are

$$u'v'_{x'} + v'v'_{y'} + w'v'_{z'} + f(u' + c_{\text{obs}}) = -\frac{P^B_{y'}}{\rho_o} - R_{y'} + \frac{\tau^y_{z'}}{\rho_o} \quad \text{and} \tag{2}$$

$$u'u'_{x'} + v'u'_{y'} + w'u'_{z'} - fv' = -\frac{P^B_{x'}}{\rho_o} - R_{x'} + \frac{\tau^x_{z'}}{\rho_o}, \tag{3}$$

where u', v', and w' are the alongshore, cross-shore, and vertical velocities, f is the Coriolis parameter, P^B is the bottom pressure, $R = \int_{-h}^{z'} (g\rho/\rho_o)\, dz$ is the buoyancy force integrated from the seafloor to elevation z' above the seafloor, g is gravitational acceleration, ρ is density, $\rho_o = 1023$ kg m^{-3} is a reference density, h is water depth, and τ^x and τ^y are the alongshore and cross-shore components of stress. Subscripts denote differentiation. Vertical flow was not measured, so terms involving w cannot be estimated. The bottom pressure measurements are too noisy to estimate accurately the alongshore bottom pressure gradient $P^B_{x'}$ over alongshore scales of a few kilometers. Estimates of the other terms are centered on a location 2 m below the mean surface at the 8-m site (see appendix).

The largest terms in the alongshore momentum balance (3), $u'u'_{x'}$ (Fig. 9a) and $R_{x'}$ (Fig. 9b), are associated with the abrupt changes in velocity and density at the front (Figs. 4 and 5). These terms approximately balance at the front, but $R_{x'}$ reaches larger values and decreases more slowly than $u'u'_{x'}$ behind the front (Fig. 9). The positive $u'u'_{x'}$ ($\approx 0.2 \times 10^{-4}$ m s^{-2}) ahead of the front,

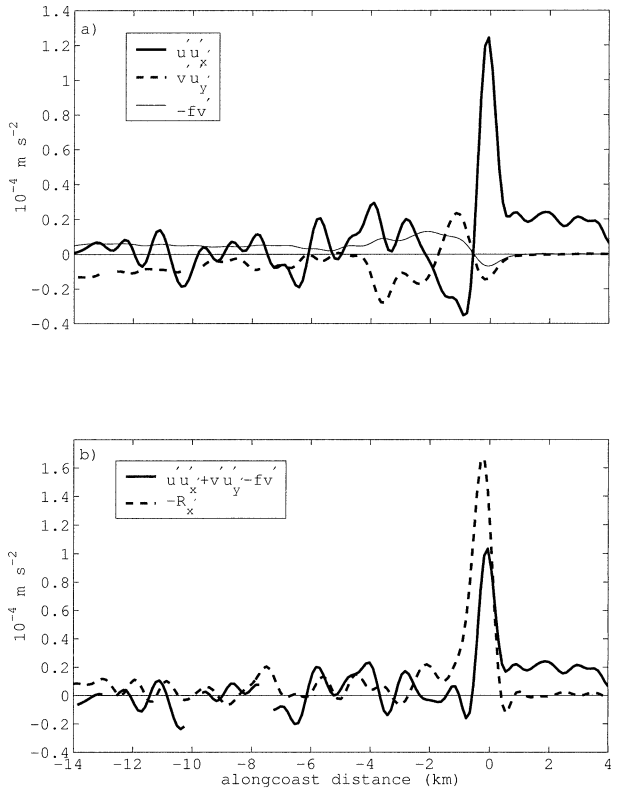

FIG. 9. Estimates of terms in the alongshore momentum balance [(2)], averaged over events 1–5, 2 m below the surface at the 8-m site vs alongshore distance: (a) advective acceleration and Coriolis terms and (b) alongshore buoyancy gradient ($-R_{x'}$), and the sum of the terms in (a).

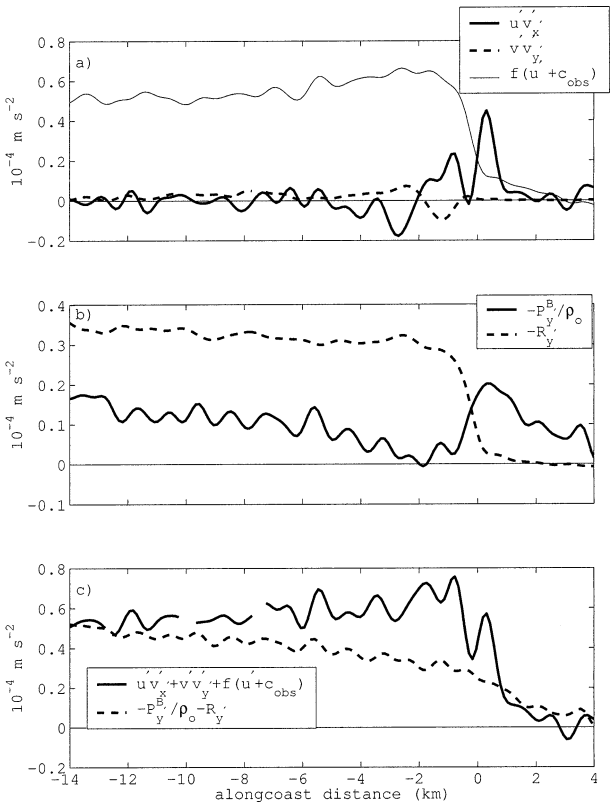

FIG. 10. Estimates of terms in the cross-shore momentum balance [(3)], averaged over events 1–5, 2 m below the surface at the 8-m site vs alongshore distance: (a) advective acceleration and Coriolis terms, (b) bottom pressure and buoyancy contributions to the cross-shore pressure gradient, and (c) the sum of the acceleration and Coriolis terms, and the total cross-shore pressure gradient.

associated with the increase in u' toward the front, presumably is balanced by an unmeasured barotropic pressure gradient corresponding to ~1 cm change in sea level over 4 km. Behind the front, $u'u'_{x'}$ and $v'u'_{y'}$ often have opposite signs and similar magnitudes (cf. solid curve with dashed curve for alongshore distances between −1 and −5 km in Fig. 9a). The Coriolis term fv' is relatively small. Rough estimates based on the bottom stress or surface stress, or consideration of the depth-averaged momentum balance (which yields similar results), suggest that the stress divergences ($\tau^x_{z'}$ and $\tau^y_{z'}$) are relatively small.

The cross-shore momentum balance both ahead of the front and more than about 5 km behind the front is approximately geostrophic [i.e., the Coriolis term $f(u' + c_{\text{obs}})$ balances the cross-shore pressure gradient $-P^B_{y'}/\rho_o - R_{y'}$; Fig. 10]. The nonlinear advective terms $u'v'_{x'}$ and $v'v'_{y'}$ are significant only near the nose (Fig. 10a), where velocity gradients are strongest. The balance is only qualitative because cross-shore velocity and pressure gradients are underestimated near the nose, which is narrower than the 5-km separation between the 5- and 21-m sites used to estimate the cross-shore bottom pressure and density gradients.

4. Discussion

The results presented here are consistent with previous observations. Propagations speeds and widths of the Chesapeake Bay buoyant coastal current during weak winds similar to those reported here have been observed with synthetic aperture radar (Donato and Marmorino 2002) and a moored array deployed in 1997 (Johnson et al. 2001). Donato and Marmorino (2002) observed a region of ''cool slick-filled water'' extending ~5 km ahead of the nose with currents measured at 5-m depth in 8 m of water that were weakly alongshore and offshore. The near-bottom alongshore velocity increased to about 25 cm s^{-1} when the front passed, similar to the observations reported here (e.g., Fig. 7a). Johnson et al. (2001) report supercritical alongshelf flows behind the Chesapeake Bay plume front from moorings along the 9-m isobath and an onshore flow reaching 25 cm s^{-1} behind the front during one event with weak winds. An abrupt increase in alongshore velocity and an offshore flow also were observed with shipboard (Yankovsky et al. 2000) and moored (Yankovsky and Garvine 1998) measurements near the nose of a Hudson River buoyant coastal current.

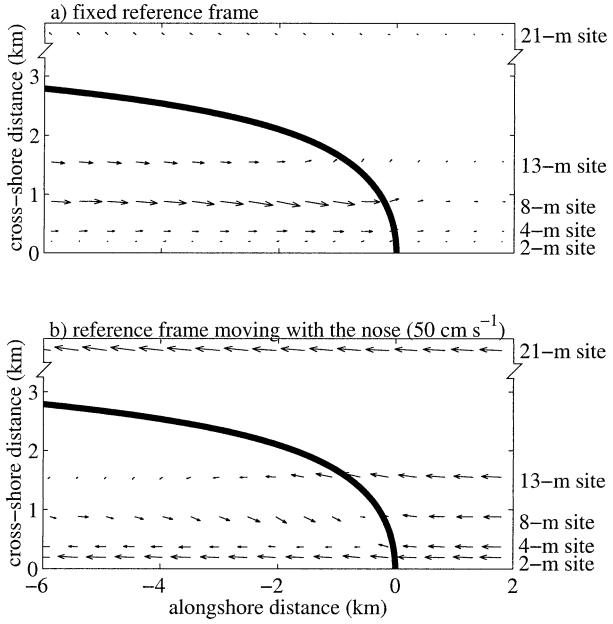

FIG. 11. Plan view of the near-surface flow field averaged over events 1–5 in (a) a fixed reference frame and (b) a reference frame moving with the front (c_{obs} in Table 1). Measurement sites are noted on the right. There are breaks in the cross-shore axes. The 21-m site is 5.6 km offshore.

The present observations show that moderate winds and surface gravity waves alter the characteristics of buoyant coastal currents, particularly the flow field near the nose. Moderate to strong upwelling-favorable winds disperse buoyant coastal currents offshore (Rennie et al. 1999; Fong and Geyer 2001; Johnson et al. 2001). During events 6–9 (Table 1) with stronger downwelling-favorable (i.e., southward) winds and more energetic surface gravity waves, the salinity front was broader, with less-well-defined boundaries. During strong downwelling-favorable winds, the flow field was more variable than during weak winds, with no consistent pattern in both cross-shore velocities near the front at any site and in alongshore velocities at the 2- and 4-m sites (where wave breaking sometimes forced strong alongshore currents). At the 8- and 13-m sites, alongshore velocities usually increased in the direction of plume propagation as the front passed, but the flow structure and magnitude varied from event to event. Near-bottom flows associated with buoyant current events 1–5 are weak, less than approximately 10 cm s^{-1} (Figs. 7 and 8), and frictional bottom stresses are relatively small. Strong wind- and breaking-wave-driven alongshore flows observed near the seafloor at other times (not shown) are largely frictionally balanced (Feddersen et al. 1998; Lentz et al. 1999; Ruessink et al. 2001).

The flow field near the nose of the Chesapeake Bay coastal current (Fig. 11) resembles the flows suggested by the theory (Fig. 1b) and laboratory experiments of Lentz and Helfrich (2002; their Figs. 13–15). Based on the scaling of Lentz and Helfrich (2002), the nondimensional variable $c_w/c_\alpha < 1$ for "surface-trapped" and $c_w/c_\alpha > 1$ for "slope-controlled" buoyant coastal currents, where $c_w = \sqrt{g'h_p}$ is an internal wave speed, $c_\alpha = \alpha g'/f$ is a topographic wave speed, $g' = g\Delta\rho/\rho_o$ is reduced gravity, $\Delta\rho$ is the density difference between the buoyant and ambient fluid, $h_p \approx 8$ m is the depth at which the plume front intersects the seafloor, $\alpha = 0.008$ is the bottom slope, and $f = 0.9 \times 10^{-4}$ s^{-1}.

Using the observed density differences (Table 1) and the parameter values listed above, $c_w/c_\alpha \approx 0.2$ for these five events, indicating that these Chesapeake Bay buoyant coastal currents are closer to a surface-trapped gravity current than to a slope-controlled gravity current, consistent with the observation that only about one-fourth of the width of the buoyant current is in contact with the seafloor (Fig. 2b). The predicted propagation speed c_p, approximately equal to $c_w/(1 + c_w/c_\alpha)$, is 35 cm s^{-1}, smaller than the observed speed ($\sim$50 cm s^{-1}), and the predicted width W_p, approximately equal to $c_w(1 + c_w/c_\alpha)/f$, is 5.7 km, larger than the observed width ($<$4 km). The maximum alongshore flow occurs in $\sim$8-m water depth (Figs. 5 and 11a), near the intersection of the front with the seafloor (Fig. 2b), consistent with the Lentz and Helfrich (2002) theory (Fig. 1b). The predicted ratio of the alongshore flow behind the front to the propagation speed is $1 + c_w/c_\alpha \sim 1.2$ for the Chesapeake events, similar to the observed ratio of about 1.5 observed at the 8-m site 1 km behind the front. Within the buoyant plume, the observed alongshore flow decreases toward the coast, in agreement with laboratory observations (Lentz and Helfrich 2002). The observations suggest the alongshore flow decreases offshore of where the plume intersects the seafloor ($\sim$8-m depth, about 1 km from shore; Fig. 11a), similar to laboratory experiments (Stern et al. 1982; Griffiths and Hopfinger 1983; Lentz and Helfrich 2002). However, currents were not observed within 4 m of the surface at the 13-m site, and there are no current observations between the 13-m site about 1.5 km offshore and the 21-m site about 5 km offshore (where the coastal current was not detected; Fig. 2b).

As suggested by Lentz and Helfrich (2002), onshore flow observed behind the front (Figs. 6c,d) supplies buoyant water to the nearshore region where the alongshore flow is weak (Figs. 5a,b). The alongshore scale of the adjustment region behind the front, estimated from the adjustment timescale $t_{adj} = 2c_w/fc_\alpha$ multiplied by the propagation speed scale c_p (Lentz and Helfrich 2002), is $L_{adj} \sim 1.6$ km, about one-half of the observed adjustment scale at the 8-m site (where the flow adjusts to a roughly constant value about 4 km behind the front; Figs. 6c and 7b).

5. Summary

During five buoyant coastal current events observed 90 km south of Chesapeake Bay when wind and surface wave forcing were weak, the density was salinity con-

trolled, and the nose of the buoyant coastal current propagated alongshore (toward the south) at about 50 cm s^{-1}. Near the nose, the buoyant coastal currents were less than 5 km wide at the surface, and the front intersected the seafloor between the 5- and 10-m isobaths, about 1 km offshore (Fig. 2b). The salinity decrease at the nose was 2–4 (salinities values based on the practical salinity scale) over a few hundred meters (Fig. 4).

Water up to 4 km ahead of the propagating nose was displaced alongshore (in the direction of the buoyant current propagation) and offshore. Maximum currents ahead of the nose were observed in 8-m water depth ($\sim$20 cm s^{-1} alongshore and $\sim$10 cm s^{-1} offshore), just prior to the nose arrival (alongshore distance $\sim$0 in Figs. 5c and 6c). At the front, in 8-m water depth, the alongshore velocity increased abruptly to approximately the propagation speed of the buoyant gravity current (50 cm s^{-1}). This rapid advective acceleration of the alongshore flow at the front was balanced by the baroclinic pressure gradient across the front (alongshore distance $\sim$0 in Fig. 9b). The increase in alongshore velocity was more gradual onshore and offshore of the 8-m isobath (Fig. 5). Behind the front, the near-surface alongshore flow in 8-m water depth continued to accelerate to supercritical velocities of about 75 cm s^{-1} ($\sim$1.5 times the propagation speed). The alongshore flow behind the front was subcritical in 2- and 4-m water depth and was usually subcritical in 13-m water depth. Offshore flow (5–10 cm s^{-1}) ahead of and at the front (Fig. 6) provides a potentially important mechanism for offshore advection of nearshore water. In 8- and 13-m water depths, onshore flow of about 5–15 cm s^{-1} often extended more than 10 km behind the front (Figs. 6c,d), transporting fresh water to the region of weak, subcritical alongshore flow within a few hundred meters of the shoreline. A consistent cross-shore flow was not observed behind the front in 2- and 4-m water depth. The cross-shore momentum balance in 8-m water depth is approximately geostrophic (Fig. 10). The onshore flow and supercritical alongshore flow observed in 8-m depth, where the front intersects the seafloor, as well as the overall observed flow pattern, are consistent with theory and laboratory results for buoyant gravity currents propagating along a sloping bottom (Lentz and Helfrich 2002; cf. Fig. 11 with Fig. 1b).

Acknowledgments. Funding was provided by the National Science Foundation and the Office of Naval Research. Comments on an earlier version of the manuscript by Rich Garvine and Rocky Geyer are greatly appreciated. The Upper Ocean Processes Group at Woods Hole Oceanographic Institution prepared, deployed, and recovered the moorings and instruments at the 13- and 21-m sites. Craig Marquette was responsible for the alongshore array of pressure–temperature–conductivity instruments. The nearshore arrays were deployed and maintained by staff from the Center for Coastal Studies, Scripps Institution of Oceanography. Michael Clifton designed the instrument supporting structures at the 2-, 4-, and 8-m sites and contributed significantly to their fabrication, deployment, and maintenance. John Largier graciously provided the small boat salinity section shown in Fig. 2b. Staff from the U. S. Army Corps of Engineers Field Research Facility, Duck, North Carolina, provided excellent logistical support. Drs. T. H. C. Herbers, Edith Gallagher, and Britt Raubenheimer made valuable contributions to the field experiment.

APPENDIX

Estimating Terms in Momentum Balances with Observations

Terms in the momentum balances [(2) and (3)] were estimated using the field observations. Alongshore gradients were estimated as finite differences with $\Delta x =$ 120 m, assuming temporal variations result from alongshore spatial variations advecting past the array at the front propagation speed [(1)]. These noisy estimates were filtered using an 8-point (i.e., about 1 km or 32 min) low-pass filter. Alongshore velocity gradients and the Coriolis terms were estimated using the current observations 2 m below the surface at the 8-m site. Alongshore density gradients were estimated using the pier measurements 4 m below the surface. Cross-shore velocity gradients were estimated as differences between the 4- (2 m below surface) and 13-m (4 m below the surface) sites. Cross-shore bottom pressure and density gradients were estimated as differences between the 21-m site and the 5-m depth bottom pressure and pier density, respectively. Vertical integrals of density were estimated using trapezoidal integration of the density at four heights at the 21-m site and one (events 1,2) or two (events 3–5) heights at the pier site.

REFERENCES

Batchelor, G. K., 1981: *An Introduction to Fluid Dynamics.* Cambridge University Press, 615 pp.

Beardsley, R. C., 1987: A comparison of the vector-averaging current meter and New Edgerton, Germeshausen, and Grier, Inc., vector-measuring current meter on a surface mooring in Coastal Ocean Dynamics Experiment-1. *J. Geophys. Res.,* **92,** 1845–1860.

Chao, S.-Y., 1998: River-forced estuarine plumes. *J. Phys. Oceanogr.*, **18,** 72–88.

Chapman, D. C., and S. J. Lentz, 1994: Trapping of a coastal density front by the bottom boundary layer. *J. Phys. Oceanogr.,* **24,** 1464–1479.

Donato, T. F., and G. O. Marmorino, 2002: The surface morphology of a coastal gravity current. *Cont. Shelf Res.,* **22,** 141–146.

Elgar, S., R. T. Guza, B. Raubenheimer, T. H. C. Herbers, and E. L. Gallagher, 1997: Spectral evolution of shoaling and breaking waves on a barred beach. *J. Geophys. Res.,* **102,** 15 797–15 805.

Feddersen, F., R. T. Guza, S. Elgar, and T. H. C. Herbers, 1998: Longshore momentum balances in the nearshore. *J. Geophys. Res.,* **103,** 15 667–15 676.

Fong, D. A., and W. R. Geyer, 2001: Response of a river plume during an upwelling favorable wind event. *J. Geophys. Res.,* **106,** 1067–1084.

——, and ——, 2002: The alongshore transport of freshwater in a surface-trapped river plume. *J. Phys. Oceanogr.,* **32,** 957–972.
Garvine, R. W., 1999: Penetration of buoyant coastal discharge onto the continental shelf: A numerical model experiment. *J. Phys. Oceanogr.,* **29,** 1892–1909.
Griffiths, R. W., and E. J. Hopfinger, 1983: Gravity currents moving along a lateral boundary in a rotating frame. *J. Fluid Mech.,* **134,** 357–399.
Guza, R. T., M. C. Clifton, and F. Rezvani, 1988: Field intercomparisons of electromagnetic current meters. *J. Geophys. Res.,* **93,** 9302–9314.
Hill, A. E., 1998: Buoyancy effects in coastal and shelf seas. *The Sea,* K. H. Brink and A. R. Robinson, Eds., *The Global Coastal Ocean, Processes and Methods,* Vol. 10, John Wiley and Sons, 21–62.
Johnson, D. R., A. Weidemann, and R. Arnone, 2001: Chesapeake Bay outflow and plume and coastal upwelling events: Physical and optical properties. *J. Geophys. Res.,* **106,** 11 613–11 622.
Kourafalou, V. H., L.-Y. Oey, J. D. Wang, and T. N. Lee, 1996: The fate of river discharge on the continental shelf. 1. Modeling the river plume and the inner shelf coastal current. *J. Geophys. Res.,* **101,** 3415–3434.
Lentz, S. J., 2001: The influence of stratification on the wind-driven cross-shelf circulation over the North Carolina shelf. *J. Phys. Oceanogr.,* **31,** 2749–2760.
——, and K. R. Helfrich, 2002: Buoyant gravity currents along a sloping bottom in a rotating fluid. *J. Fluid Mech.,* **464,** 251–278.
——, R. T. Guza, S. Elgar, F. Feddersen, and T. H. C. Herbers, 1999: Momentum balances on the North Carolina inner shelf. *J. Geophys. Res.,* **104,** 18 205–18 226.
——, M. Carr, and T. H. C. Herbers, 2001: Barotropic tides on the North Carolina shelf. *J. Phys. Oceanogr.,* **31,** 1843–1859.
Luketina, D. A., and J. Imberger, 1987: Characteristics of a surface buoyant jet. *J. Geophys. Res.,* **92,** 5435–5447.
Marmorino, G. O., and C. L. Trump, 2000: Gravity current structure of the Chesapeake Bay outflow plume. *J. Geophys. Res.,* **105,** 28 847–28 861.
O'Donnell, J., G. O. Marmorino, and C. L. Trump, 1998: Convergence and downwelling at a river plume front. *J. Phys. Oceanogr.,* **28,** 1481–1495.
Rennie, S. E., 1997: Wind interaction with buoyant plumes on the inner shelf. Ph.D. thesis, College of William and Mary, 166 pp.
——, J. L. Largier, and S. J. Lentz, 1999: Observations of low-salinity coastal current pulses downstream of Chesapeake Bay. *J. Geophys. Res.,* **104,** 18 227–18 240.
Ruessink, B. G., J. R. Miles, F. Feddersen, R. T. Guza, and S. Elgar, 2001: Modeling the alongshore current on barred beaches. *J. Geophys. Res.,* **106,** 22 451–22 463.
Stern, M. E., J. A. Whitehead, and B. L. Hua, 1982: The intrusion of the head of a gravity current along the coast of a rotating fluid. *J. Fluid Mech.,* **123,** 237–266.
Whitehead, J. A., and D. C. Chapman, 1986: Laboratory observations of a gravity current on a sloping bottom: The generation of shelf waves. *J. Fluid Mech.,* **172,** 373–399.
Yankovsky, A. E., and D. C. Chapman, 1997: A simple theory for the fate of buoyant coastal discharges. *J. Phys. Oceanogr.,* **27,** 1386–1401.
——, and R. W. Garvine, 1998: Subinertial dynamics on the inner New Jersey shelf during the upwelling season. *J. Phys. Oceanogr.,* **28,** 2444–2458.
——, ——, and A. Munchow, 2000: Mesoscale currents on the inner New Jersey shelf driven by the interaction of buoyancy and wind forcing. *J. Phys. Oceanogr.,* **30,** 2214–2230.